LLNL-TR-791617

Lawrence Livermore
National Laboratory

Alloying titanium and niobium via electron beam cold hearth melting

March 4, 2020

Disclaimer

Lawrence Livermore National Laboratory is operated by Lawrence Livermore National Security, LLC, for the U.S. Department of Energy, National Nuclear Security Administration under Contract DE-AC52-07NA27344.

LLNL-TR-791617
Issued: 9/27/19
Approved for public release;
distribution is unlimited.

Alloying titanium and niobium via electron beam cold hearth melting

A. S. Wu
S. G. Torres
T. P. Pluschkell
A. DeMint (Y-12)
B. R. Shelly
J. I. Jones
T. Boutaleb
J. Flinsbach (ALD)
R. McKoon
S. C. Burke
J. Dixon
A. T. Mycroft
M. A. Linne
F. J. Ryerson
E. M. Sedillo
C. Jackson
B. Bridges (Y-12)
M. W. Wraith
A. V. Hamza
G. H. Campbell
W. McLean

Acknowledgements

This research was performed at the request of Brittany Boser, Casey Deering, Jessica Farrell, Savannah Fitzwater (NA-195) and Douglas Burkes (PNNL/NA-195) in support of the LLNL and Y-12 electron beam cold hearth melting program. The authors wish to acknowledge IMR Test Labs for chemical analyses and Rob Haun for scientific expertise on Ti-Nb processing. Electron beam cold hearth melting was performed by ALD Vacuum Technologies GmbH and the authors wish to acknowledge Ralf Denger for project management, Arno Niebling for equipment design, Wolfgang Bott, Ulrich Biebricher and Ronald Creed for collaboration, design iteration and scientific discussions.

Abstract

Electron beam cold hearth melting of titanium and niobium was performed to assess the feasibility of this technique for uranium processing and to determine system requirements for LLNL applications. The demonstration consisted of (1) alloying titanium and niobium, (2) feeding and melting scrap of various forms and (3) consolidating powder feedstock. Emphasis was placed on the former, with focused efforts to produce and deliver stoichiometric amounts of titanium and niobium to the hearth for alloying. This effort demonstrated the ability to melt via electron beam and cast titanium into a thin-walled (~0.06”) niobium tube. This process was performed repeatably and an optimal set of operational parameters was identified through an iterative approach. Three alloyed ingots were produced using niobium tubes filled with titanium, by casting and slip-fit. The alloyed ingots were characterized using multiple approaches and were shown to be comprised of columnar grains, low inclusion amounts and a small degree of ordered (center to edge, top to bottom) variation in niobium concentration. Based on these findings, it is concluded that alloying can be accomplished in a single step, without the need for an additional melting step after electron beam cold hearth melting. Details of these analyses, along with efforts to adopt cold hearth melting technology for scrap and powder recycle are provided herein.

Table of Contents

Table of Figures

Table of Tables

Abbreviations

AES	Atomic emission spectroscopy
ALD	ALD Vacuum Technologies GmbH
CHM	Cold Hearth Melter
cc	Cubic centimeter
D	Diameter
DU	Depleted uranium
EB	Electron Beam
EDS	Energy dispersive X-ray spectroscopy
H	Height
ICP	Inductively coupled plasma
IGF	Inert gas fusion
in	Inches
L	Length
LLNL	Lawrence Livermore National Laboratory
mm	Millimeter
µm	Micrometer
MS	Mass spectroscopy
Nb	Niobium
SEM	Scanning electron microscope
SS	Stainless steel
T	Thickness
Ti	Titanium
U-6Nb	Uranium-6 wt.% Niobium
VIM	Vacuum induction melting
W	Width
WDS	Wavelength dispersive X-ray spectroscopy
XRF	X-ray fluorescence
Y-12	Y-12 National Security Complex

Section 1

Objectives and Statement of Work

LLNL explored electron beam cold hearth melting (CHM) technology for uranium-6 weight percent niobium (U-6Nb) recycling from 1993-1997. The study produced CHM ingots which met or exceeded chemical specifications for elemental impurity content and Nb homogeneity [1-3], concluding that EB CHM technology offers a viable, single-step process to recycle U-6Nb scrap metal. During this time, alloying of depleted uranium (DU) and Nb was also explored [2].

In a continuation of this effort, LLNL and Y-12 National Security Complex (Oak Ridge, TN) have contracted with an experienced industrial partner to design and build a CHM system capable of meeting LLNL throughput and safety requirements and performing proof-of-concept demonstrations [4]. This report describes demonstrations to assess electron beam cold hearth melting feedstock opportunities and process parameters for DU and Nb alloying. Specific CHM demonstrations discussed include:

- Feedstock preparation for alloying
- Substitute, non-radioactive material (titanium) alloying with Nb
- Scrap feeding and melting
- Powder consolidation

These demonstrations were funded by NNSA/NA-192 and performed by ALD Vacuum Technologies GmbH (Hanau, Germany).

1.1 Alloying Demonstration

1.1.1 Material Selection

The Ti-Nb binary alloy was selected to demonstrate alloying via EB CHM. The Ti-Nb and U-Nb phase diagrams are shown in Fig. 1.1. Ti-14 at.% Nb forms an equilibrium BCC solid phase >700°C, which transforms martensitically by quenching into the α'- HCP phase at low Nb content and into the orthorhombic distortion of the HCP phase (α") at higher Ti content [5]. U-6Nb forms an equilibrium BCC solid phase > 640°C, which transforms martensitically by quenching into the distorted α'-orthorhombic phase at low Nb content and into the distorted α"-monoclinic phase at higher Nb content [6]. The solidification behavior is similar due to the higher melting point of Nb compared with U and Ti.

The ability of the Ti-Nb system to capture the kinetics, martensite formation and crystallographic phase behavior of the U-Nb system is known and has been explored for this purpose previously [7]. Furthermore, the kinetics of the Ti-Nb system is well-characterized and documented [8]. CHM of Ti is an industry standard due to its reactivity and vapor pressure [9].

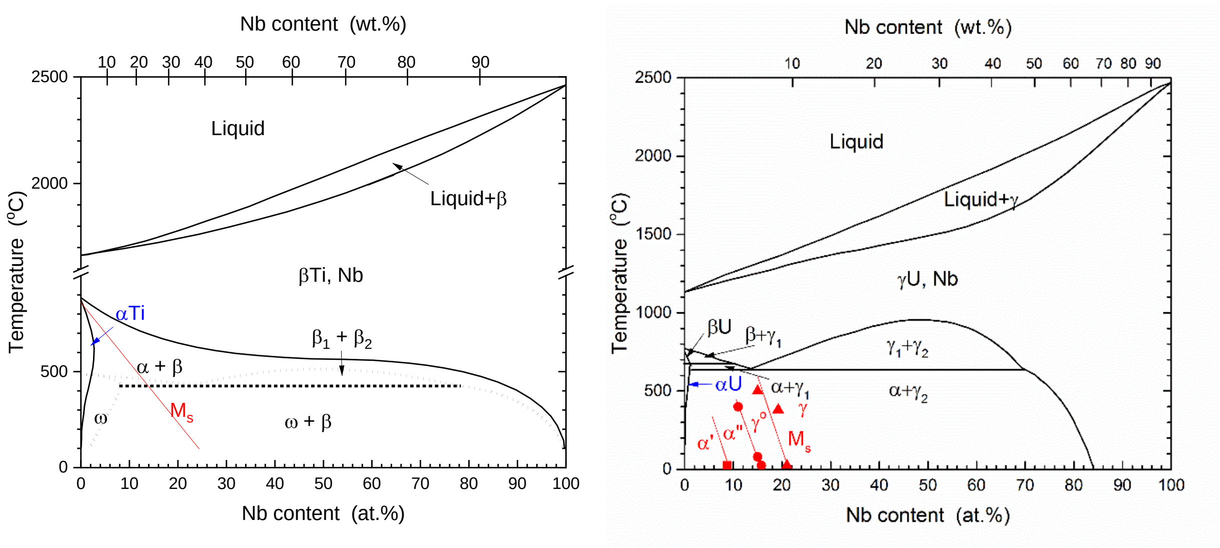

Fig. 1.1. (left) Nb-Ti phase diagram redrawn from [5] (right) Nb-U phase diagram redrawn from [10]

1.1.2 Alloying Method

Titanium metal was EB melted in a water-cooled copper hearth and cast into Nb tubes (2” ID) of different lengths. This approach mimics our intended process of melting depleted uranium into Nb tubes. The tubes were inspected for casting porosity and defects. Alternative methods of feeding a stoichiometric ratio of elements for alloying include feeding single-element rods of different sizes and feeding in chopped metal.

During EB CHM, rastering patterns were implemented and tuned to provide sufficient mixing at specified volume contents. CHM employs a semi-continuous casting process—solid metal is fed into a hearth, melted and mixed by an electron beam, then poured into a water-cooled copper ingot crucible. The process is halted for ingot withdrawal, which is performed without venting the vacuum chamber. Recommendations for EB CHM process parameters and hearth design were made by ALD, based on these demonstrations.

1.1.3 Assessment and Process Design

Materials characterization on Ti-Nb ingots and Ti-filled Nb tubes was performed to verify global and local chemical content and to assess solidification microstructures and degree of banding. This study required metallographic analysis including optical and electron microscopy, electron microprobe analysis for microscale chemical segregation, inert gas fusion for carbon, oxygen, nitrogen, sulfur and hydrogen impurities, and inductively coupled plasma mass spectroscopy (ICP-MS) and atomic emission spectroscopy (ICP-AES) for global chemical composition. The data indicate that CHM alloyed Ti and Nb with reasonable success marked by small variations in Nb macroscale distribution.

1.2 Scrap Processing Demonstration

This effort addressed a non-standard approach to feeding scrap metal into the CHM chamber. Typically, a scrap conveyor (vibratory or auger) would be used for this purpose. In this demonstration, scrap of varying dimensions was conveyed using a bar feed system and observations on methods to improve scrap delivery using this accessory were made. This was explored as a cost/space savings measure.

Note that CHM offers some opportunities to refine or purify scrap metal. This has been accomplished through (1) vapor pressure separation, chemisorption [11, 12] and (2) density separation. The former refers to the vaporization of high vapor pressure impurities, relative to the vapor pressures of the primary feedstock constituents [13]. In the latter instance, lower density inclusions, such as oxides or carbides form a slag at the top surface of the molten metal in the hearth. This slag is manipulated and prevented from entering the crucible through a convoluted hearth design [14], weir or dam blocking or electron beam rastering. In the case of higher density impurities (tungsten carbide in Ti alloys is a common example), hearth designs which allow sufficient time for the high-density impurities to settle and prevent these impurities from entering the crucible can be employed. Recycling was not addressed during this demonstration; however, it will be a topic of future effort.

1.3 Powder Consolidation

Three powder feedstock trials were conducted to determine the viability of CHM for reprocessing metal in powder form. The main driver for this effort is the potential to recycle scrap from the laser powder bed fusion additive manufacturing (AM) process. The initial trial attempted to feed powder via an overhead vibratory feed attachment, the second trial attempted to melt powder directly within a consolidation hearth to create a slab casting, and the final trial used a consolidation hearth to melt an aggregate mixture of powder and solid AM support structure.

The first two trials proved unsuccessful, as metal powder has low thermal conductivity and tended to vaporize upon contact with the electron beam. This resulted in the dispersal of powder within the melt chamber. The third test was met with some success as ~90% of the powder and AM support material was melted and recovered. The remaining ~10% consisted of splatter, melted casting chunks which separated from the main slab, and un-melted powder which was dispersed throughout the chamber.

1.4 Closing Introductory Remarks

This effort serves to (1) identify potential feedstock forms for future DU and Nb processing, (2) familiarize LLNL and Y-12 personnel with CHM process design, procedures and products, and (3) develop a CHM system capable of meeting LLNL processing demands and safety requirements.

Section 2

Feedstock Preparation for Alloying

Electron beam CHM can process metal in various forms, including bulk (ingots, full-sized components), discontinuous (chopped components, briquettes) and fines (machining chips, powder with caveats—see Appendix A). Various feedstock materials and forms were purchased and prepared for CHM demonstrations. These include rods, tubes, chopped components and powder.

Considerations for alloying titanium (as a substitute test material for depleted uranium) with niobium include available material forms and maintaining a stoichiometric ratio of Nb with Ti. Specific considerations for alloying DU and Nb are similar. DU is available as bulk scrap and derby. Derby requires size reduction and a vacuum induction melting step to refine impurities from the bomb reduction process. CHM feedstock forms must be able to produce alloyed ingots with approximately 6 wt.% Nb and a DU balance. No impurities, specifically carbon, should be added during processing.

Based on prior experience melting and casting DU into Nb tubes [2], Ti-filled Nb tubes were selected as the feedstock for the Ti-Nb alloying demonstration. Two approaches were pursued to produce this feedstock geometry; these are described in the following subsections.

2.1 Feedstock 1: Ti-Filled Nb Tubes

2.1.1 Material Form

A set of 21 Nb tubes and 23 Ti rods were ordered from Admat, Inc. (Norristown, PA). Eleven Nb tubes were capped off on one end by fabrication of a "cup" from .040" niobium sheet. The "cup" was ~1/8" L, with a flat bottom, formed to a tight fit on the ID of the niobium tube. Special Metals, Inc. (Willis, TX) performed a fusion only weld of the cup to the sleeve in an inert atmosphere (Fig. 2.1). Additional Nb tubes and Ti rods were purchased as back-up from Stanford Advanced Materials (Lake Forest, CA), see Fig. 2.2. Dimensions and material grade information for each of the raw materials are provided in Table 2.1.

Fig. 2.1. Photograph of Ti rods and Nb tubes from Admat

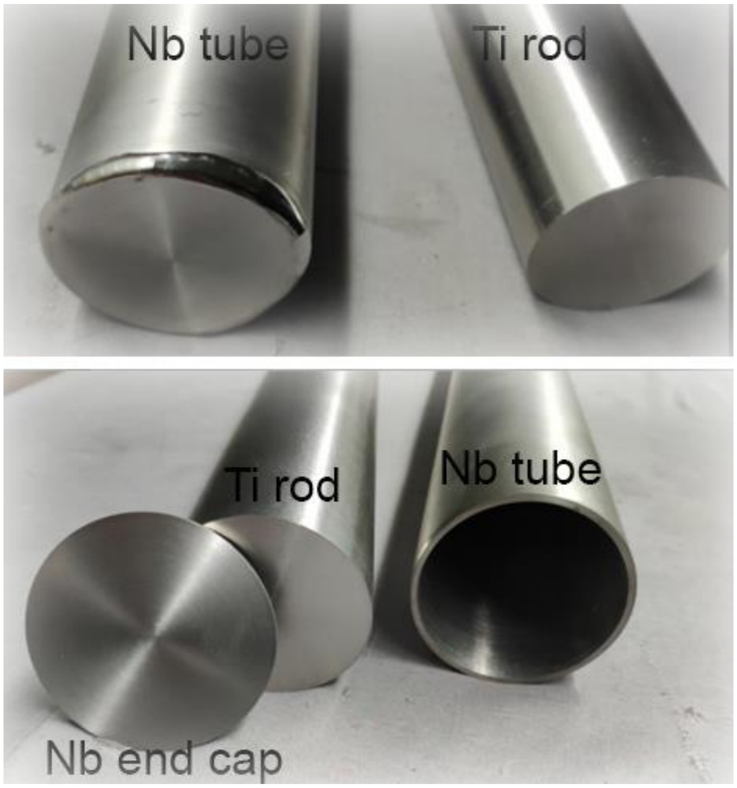

Fig. 2.2. Photograph of Ti rods and Nb tubes from Stanford Advanced Materials

Table 2.1. Feedstock materials provided to ALD for processing via CHM

Form	Quantity	Dimensions	Material grade	Supplier
Ti rods	23	2’ L, 2” D	ASTM B265 Grade 1	Admat, Inc.
Ti rods	12	1’ L, 1.819” D	ASTM B265 Grade 1	Stanford Advanced Materials
Nb tube	21	2’ L, 2” ID, 2.13” OD	Reactor Grade	Admat, Inc.
Nb tube	12	1’2” L, 2” ID, 2.16” OD	99.9%	Stanford Advanced Materials
Nb sheet (for end caps)	11	.040" T	99.9%	
Ti coins	~30 kg	2.75” D, 3/16” T, 4” radius curvature	ASTM B265 Grade 2	
Ti porous scrap	~10 kg	<2.75” x <24”, 3/16” T, 4” radius curvature	ASTM B265 Grade 2	
SS powder	25 kg	<100 µm D	316L	

2.1.2 Melting and Casting

In preparation for Nb tube filling, a 1’ long Nb tube was loaded into the crucible chamber and supported by the dovetail starter installed on the withdrawal mechanism. A graphite blank was machined with a funnel with a diametrical taper to approximately 2.2” to accommodate the open top end of the Nb tube (Fig. 2.3). The 3 mm gap between the graphite mold and Nb tube outer wall was filled with graphite foil.

Four 2’ long Ti rods were loaded into a bar feeder system capable of delivering two rods into the chamber simultaneously. The hearth was clean and empty prior to Ti melting. After the furnace was evacuated, the Ti rods were melted using one of the chamber’s two EB guns (300 kW) guns following a hearth refining pattern, which allowed a small cold weir to form in the v-notched spout of the hearth. Once enough liquid volume was melted in the hearth (Fig. 2.4), the EB was directed to melt the weir, allowing material to flow into the Nb tube. The liquid pool volume was able to fill the Nb tube in a single pour.

Four subsequent tubes were filled in a similar manner, with minor process improvements made after each trial.

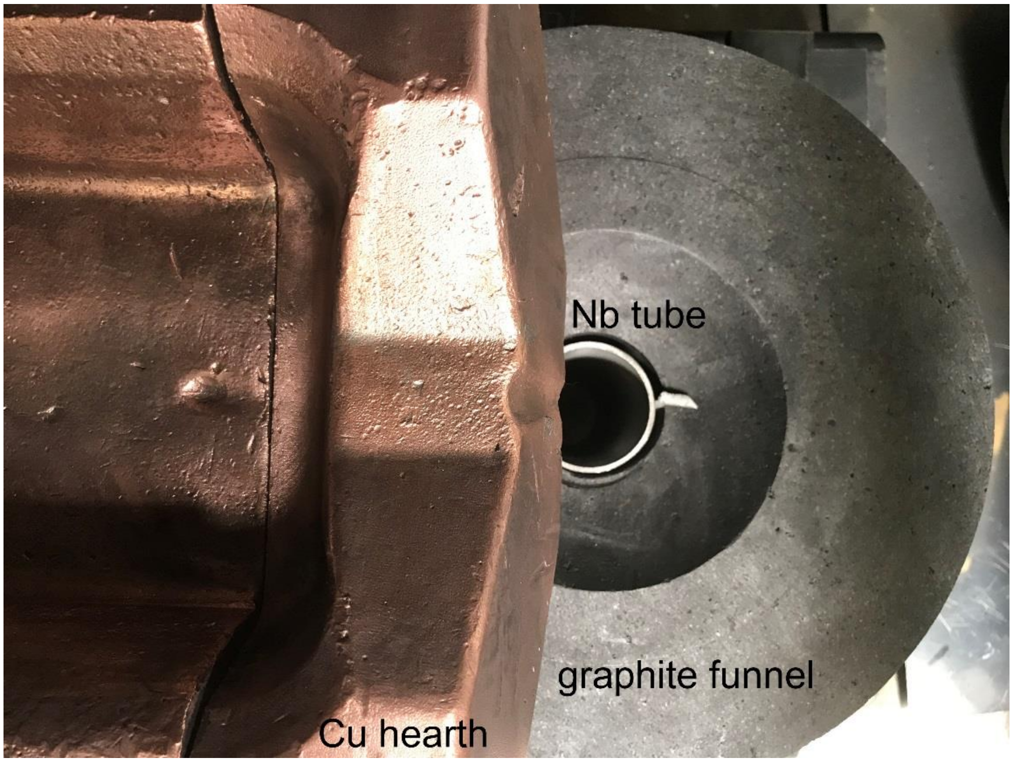

Fig. 2.3. Photograph of hearth alignment with graphite funnel for Nb tube filling demonstrations

During the second trial, the Nb tube position was adjusted with respect to the v-notch hearth lip and the Nb tube was preheated with the EB, resulting in a slight improvement in tube fill. The following three trials were performed using a 2’ long Nb tube. Since these tubes have a slightly larger OD, no graphite foil was needed to shim the gap between the tube and graphite funnel. During the third trial, two liquid Ti pours were needed to fill the Nb tube. Before the fourth trial, the Nb tube was re-positioned to improve metal flow into the tube; this resulted in a smaller crown or mushroom (i.e., material overflow contained by the graphite funnel after filling the Nb tube—see Fig. 2.5a, 2.5c). An image of two rods after EB melting is provided in Fig. 2.5b. In the fifth trial, the EB current was increased for a brief period, resulting in overheating and melting of the Nb tube.

In summary, two 1' long and three 2' long Ti-filled Nb tubes were prepared, yielding five tubes in total. Mass balances for the first Nb tube filling demonstration are provided in Table 2.2. Note that hearth filling accounts for some of the mass loss during Tube 1 filling.

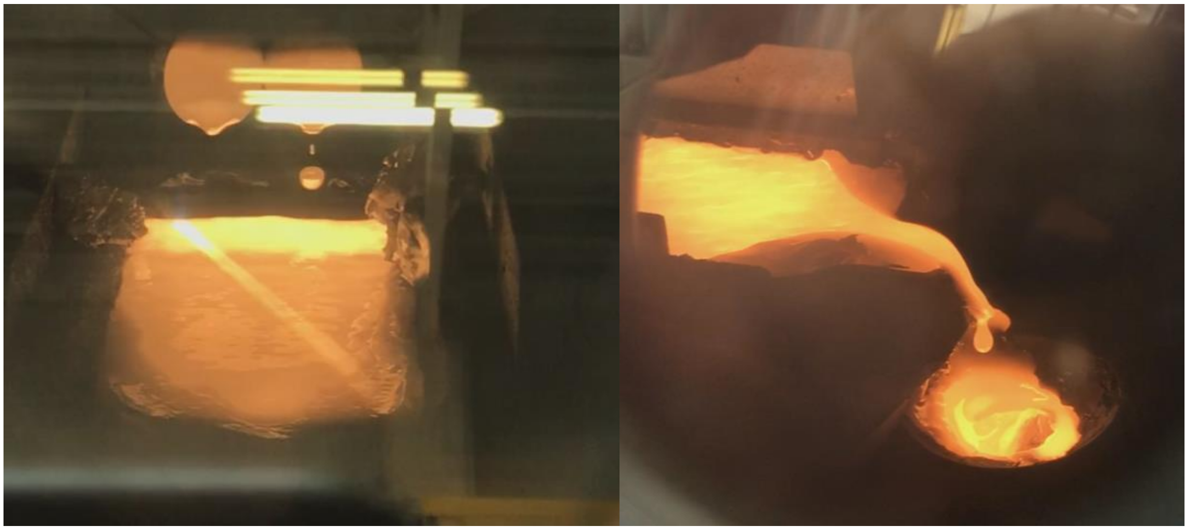

Fig. 2.4. Photographs of the vacuum furnace chamber during CHM Ti bar melting and hearth filling; horizontal lines from glare/reflection of light off the leaded viewport (left) and casting after dam melting (right)

Table 2.2. First fill tube trial (1' long Nb tube) mass balance (all numbers in g unless otherwise specified) [15]

Material	Tube 1		Tube 2		Tube 3		Tube 4		Tube 5	
	Input	Output	Input	Output	Input	Output	Input	Output	Input	Output
Ti rod	21810	8245	10930	5820	16740	9593	9583	4475	15394	5714
Nb tube	849		849		1478		1480		1479	
Filled tube after cutting		3043		3059		6412		6494		4520
Crown		199		231		1.42		316		5150
Hearth										9775
End cap						46		58		1525
Totals	22659	11487	11779	9110	18218	16052	11063	11343	16873	26684
Loss	7.3% total									

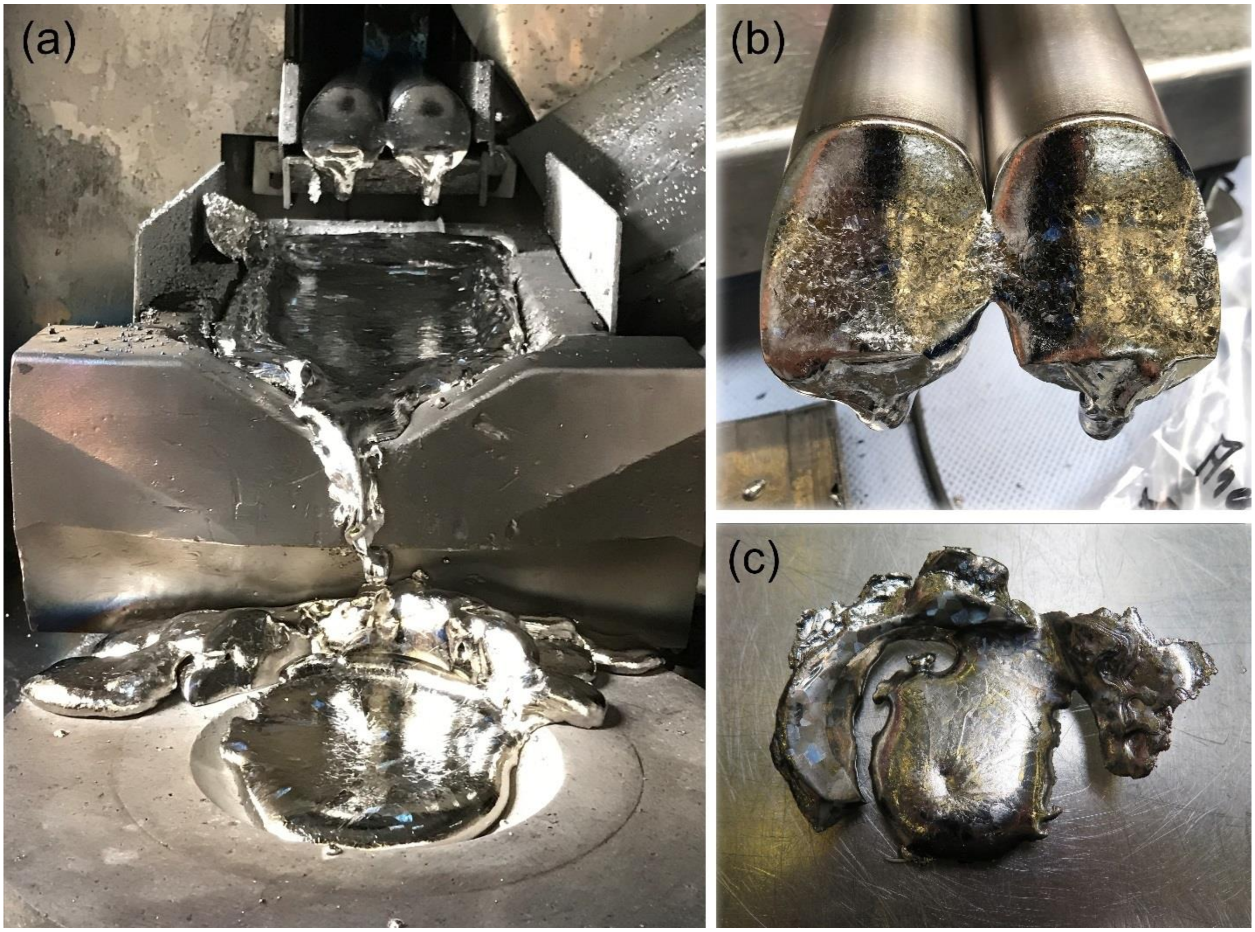

Fig. 2.5. Photographs depicting (a) solidified metal in the hearth and on top of the graphite funnel, (b) partially melted Ti bars and (c) solidified Ti metal extending from the top opening of the Nb tube, referred to as a crown

2.1.3 Comments on Ti-Filled Nb Tube Quality

Each Ti-filled Nb tube was cooled then removed from the ingot chamber and the top and bottom ends were sawed off. Visual inspection of a cross-sectioned Ti-filled Nb tube revealed a small amount of void space, but an otherwise complete fill (Fig. 2.6). The material balances are provided in Table 2.3. Note that the lengths are overestimated, resulting in an overestimated void space. Overall, the best fill was achieved in Tubes 3 and 4. These were used as feedstock for the Ti-Nb alloying demonstration. The remaining three tubes were retained for analysis. Note that Tube 5 was not completely filled due to some Nb tube melting.

Fig. 2.6. Photographs of cross-sectioned Ti-filled Nb tubes showing reasonable fill, with larger voids present near top and bottom of Tube 1 (left) and smaller voids present along the length of Tube 2 (right)

Table 2.3. Calculated density/void space in the Ti-filled Nb tubes [16]

	L (in)	ID (in)	OD (in)	Total cut mass (meas) (g)	Nb mass (calc) (g)	Ti mass (calc)	Ti mass needed (calc)	% Ti fill	% void in Ti fill
Tube 1*	12	1.85	1.98	3043	715	2328	2383	97.7	2.3
Tube 2*	12	1.85	1.98	3059	715	2344	2383	98.4	1.6
Tube 3	22.8	1.98	2.13	6412	1580	4832	5168	93.5	6.5
Tube 4	23.3	1.98	2.13	6494	1615	4879	5281	92.4	7.6
Tube 5*	24	1.98	2.13	4520	1720	2800	5440	51.5	48.5

***Corrected for remaining end cap.**

2.1.4 Comments on Processing Time

The time required to fill each tube was approximately 30 minutes. Including CHM preparation and clean-up, three runs per day were performed during an 8 hour shift. Should LLNL pursue this route for DU-Nb feedstock preparation, multiple Nb tubes may be loaded into the crucible to improve throughput.

2.1.5 Comments on Tube Filling via CHM

A high superheat allowed the Ti to remain liquid during the tube filling and no evidence of freeze-out was observed. Process improvements to aid tube filling include heating the tube by rastering the EB over the top surface. A noteworthy process observation is that the LLNL CHM system EB gun is located directly over the crucible, meaning that the EB could potentially reach the end cap of the Nb tube. This placement of the EB gun also means that melting the dam or weir in the LLNL system will be easier due to a lack of an overhang or shadowed region.

2.2 Feasibility check: Melting and Casting DU into Nb Tube

A vacuum induction melting furnace at Y-12 was used to melt depleted uranium and cast the liquid DU into a Nb tube (1” ID, 1/32” wall thickness, ~4.5” L). The liquid DU filled the tube without significant void space without melting the Nb tube. A cross-section of the DU-filled Nb tube was polished and imaged using an optical microscope (Axio Observer.Z1/7). Some voids are observed at the DU-Nb interface; these might be eliminated through additional Nb tube cleaning steps.

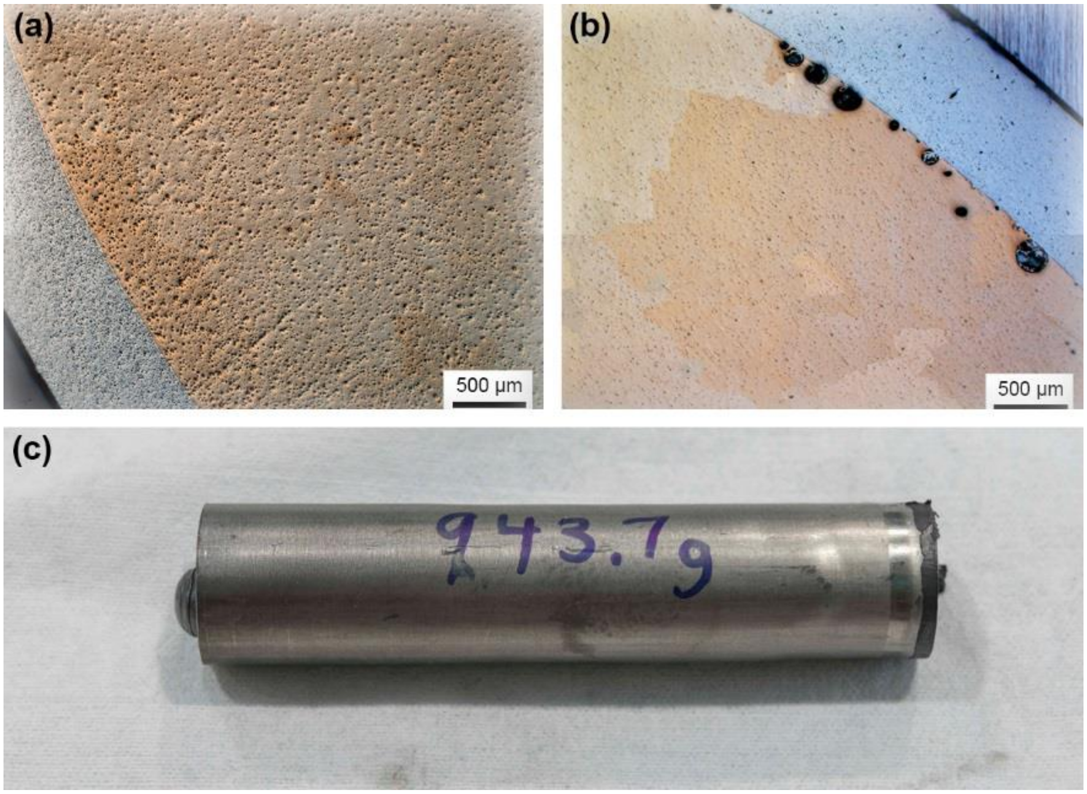

Fig. 2.7. (a-b) Optical micrographs depicting DU (orange) in a Nb (grey) tube and (c) photograph of a DU-filled Nb tube

2.3 Feedstock 2: Slip-Fit Ti Rods in Nb Tubes

The remaining 10 Nb tubes and Ti rods were tack welded in four places on both ends, leaving an unwelded area to allow gas trapped between the Nb tube and the Ti rod to escape while under vacuum during the CHM process. This was performed by Special Metals, Inc. to secure the tubes and rods during feeding into the CHM furnace chamber.

2.4 Stoichiometry

The controlled ratio of Ti to Nb is provided for each alloy feedstock in Table 2.4.

Table 2.4. Feedstock stoichiometry

	Nb mass (g)	Ti mass (g)	Wt.%Nb	Density (g/cc)
Slip-Fit Ti-Nb Feedstock	1598	4855	24.8	5.5
Ti-Filled Nb Tube Feedstock	1598	5440	22.7	5.4

Section 3

Alloying

Feedstock as described in Section 2 was used to demonstrate the ability of EB CHM to alloy Ti and Nb. Titanium is routinely alloyed in the EB CHM industry [9, 17]. This demonstration is aimed at (1) assessing the degree of segregation and microstructures in CHM alloyed Ti-Nb ingots, (2) assessing feedstock form suitability for CHM, (3) determining processing times and (4) gaining experience and familiarity with the CHM process.

3.1 Melting and Alloying

Three Ti-Nb ingots were alloyed via CHM using one 300 kW EB gun (70 kW, 2A at 35 kV directed to the hearth and 22 kW, 0.55 A at 40 kV directed to the crucible). Their dimensions and masses are provided in Table 3.1 and images of the ingots and top surfaces are provided in Fig. 3.1.

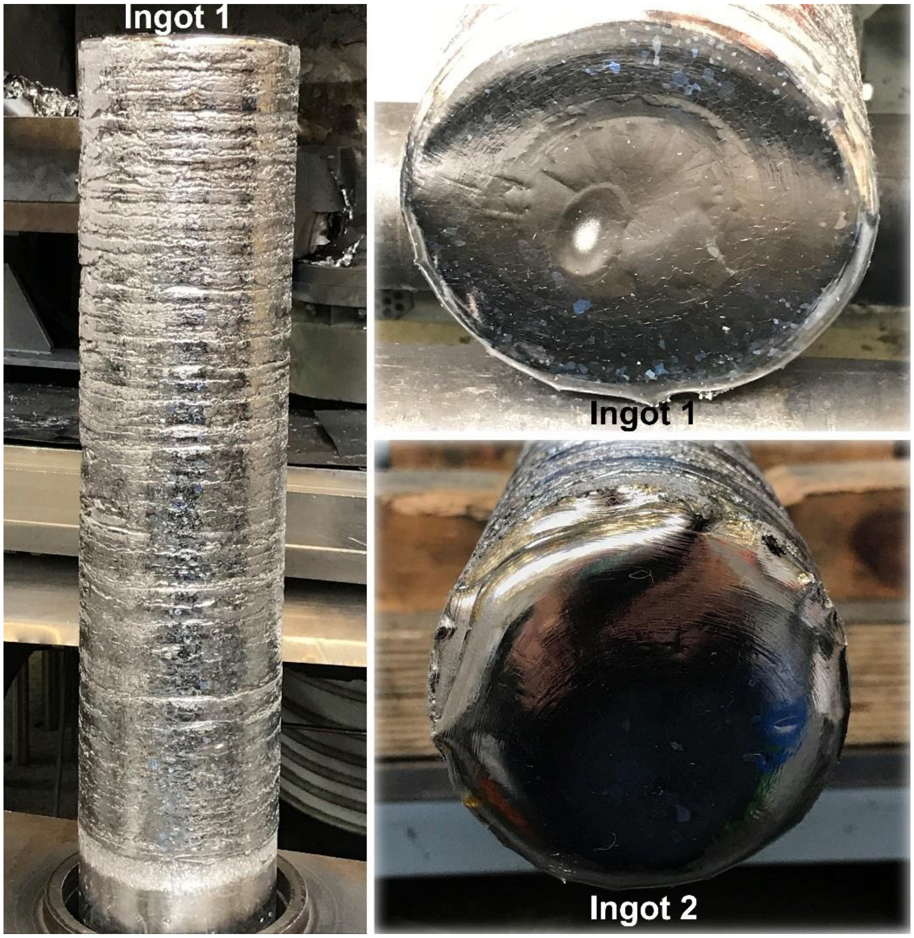

Fig. 3.1. Photographs of alloyed Ti-Nb ingots and ingot tops; note photographs were acquired with different scales

Table 3.1. Alloyed ingot feedstock and dimensions

	Feedstock form	Dimensions
Ingot 1	Ti rods slip-fit into Nb tubes (x9)	5.9” D x 22.0” L
Ingot 2	Ti-filled Nb tubes (x2)	2.5” D x 30.0” L
Ingot 3	Ti rods slip-fit into Nb tubes (x2)	2.5” D x 25.5” L

3.1.1 Mass Balances

Mass balances during the three ingot alloying demonstrations are provided in Table 3.2. Note that the hearth skull size (Fig. 3.2) is somewhat consistent (11% standard deviation) from one melt campaign to another. The material loss refers to material lost to the chamber during processing (e.g. condensate). In cases where the condensate material is valuable (Ti in this case, see Section 3.2), the material could potentially be retrieved during chamber cleaning (Fig. 3.3) and reprocessed.

Fig. 3.2. Photographs of Ti hearth from Nb tube filling (bottom) and Ti-Nb hearth from alloying (top)

Table 3.2. Alloying demonstration mass balance (all numbers in kg unless otherwise specified) [15]

Material	Ingot 1		Ingot 2		Ingot 3	
	Input	Output	Input	Output	Input	Output
Feedstock	62062		12856		13809	
ALD starter block	14820		3962		3900	3860
Ingot with starter after melt		61840		16340		

Skull including unmelted feedstock		12090	10974	10587	9002	12178
Crown				247		560
Ingot after starter removal						10100
Totals	76882	73930	27792	27174	26711	26698
% Loss	3.84		2.22		0.05	

Fig. 3.3. Photographs of condensate from Ti-Nb melting process on the chamber shroud (left) and collected during chamber cleaning (right)

3.1.2 Comments on Processing Time

3.1.2.1 Feedstock melting

At a tube melting rate of 25 mm/minute, the Nb tube remained unmelted while the Ti melted and poured into the hearth (Fig. 3.4). Slowing to a melting rate of 15 mm/minute improved the melting uniformity of the Ti-Nb tubes [15]. Nevertheless, it should be noted that there was some delayed melting of the Nb tube walls, which may result in inconsistencies in Nb concentration in Ingot 1. Efforts to minimize inconsistency between the Ti and Nb melting rates include (1) incorporating proper feeder system travel controls on the LLNL system and (2) preventing tilting of feedstock rods once they have been mostly consumed, either by welding them together or by pushing them into the hearth rapidly.

3.1.2.2 Processing Time

The operational start up time, including time required to form a hearth, melt and cast a 5.9” D x 22” L ingot, was approximately 2 hours (127 minutes, 10:28 am to 12:35 pm). Based on the material feed rate of 15 mm/minute, the 5.9” D x 22” L ingot metal was melted in 37.3 minutes. Assuming a hearth has been built up, extrapolating to an ingot sized 8.5” D x 24” L yields a melting time of 84 minutes. This melting time estimate neglects hearth formation or hearth heating, ingot cooling and removal.

For reference, in the 1990’s U-6Nb CHM recycling effort [1-3], a 8.5” D x 24” L ingot was cast in approximately 1 hour. A longer hearth dwell time and therefore longer processing time may be beneficial for alloying.

Including CHM preparation and clean-up, one 5.9” D x 22” L ingot was produced during an 8 hour shift at ALD. The process is adaptable, and alloying could be performed faster. However, it should be noted that ingot casting time and procedures can affect ingot surface finish. For example, the 2.5” D x 30” L ingots were processed in an 8 hour shift at ALD. These ingots possessed a sloppy ingot surface finish (Fig. 3.5). This can be avoided by adjusting the power output to the crucible and the ingot withdrawal speed [15].

Fig. 3.4. Photograph during CHM showing molten metal in crucible and hearth, with partially melted Ti-Nb feedstock tubes

Fig. 3.5. Ingot 2 outer surface showing irregularities due to ingot withdrawal speed

3.2 Ingot Characterization

3.2.1 Density

Ingot masses and volume are compared with calculated density in Table 3.3. Differences between the calculated and stoichiometric density are attributed to the rough ingot surface finish. While there may be voids in the ingots, the procedure of maintaining a molten pool at the top of the ingot during casting and incremental ingot filling and withdrawal are performed to minimize this. Cross-sections of Ingot 1 are shown in Fig. 3.6, with no voids evident.

Table 3.3. Measured and calculated density of Ti-Nb ingots

	Stoichiometric density (g/cc)	Mass (g)	Ideal volume (crucible volume) (cc)	Calculated density (g/cc)
Ingot 1	5.5†	47020‡	9856	4.77
Ingot 2	5.4†	12378‡	2413	5.13
Ingot 3	5.5†	10100‡	2051	4.92

†From Tables 2.4 and 3.1.
‡From Table 3.2

3.2.2 Ingot 1 Sectioning

A photograph of the top half of Ingot 1 which measured 10.5” x 5.75” x 3” is shown in Figure 3.6. Ingot 1 was cross-sectioned by ALD prior to being returned to LLNL. The bottom “B” half of Ingot 1 was further sectioned by LLNL using a Struers Discotom-5 cut-off saw with a diamond cut-off wheel (M0D25) as shown in Fig. 3.7. Three one-inch slices were cut, 1” from the top, 1” from the bottom and 4.5” from the top (5.5” from the bottom). Each of the three slices were cut in half and 1” x 1” cubes were cut from each slice and labeled C (center), M (middle) and E (edge) as shown in Fig. 3.7 and 3.8. Each of the 1” x 1” cubes were further sectioned in the radial and longitudinal directions. Sectioning of the top and bottom quadrants of Ingot 1, labeled as “A Top” and “A Bottom”, was performed by IMR Test Labs, Lansing, NY (Fig. 3.9).

Fig. 3.6. Photograph of the top half of Ingot 1, measuring 10.5” x 5.75” x 3” after cross-sectioning via wet saw

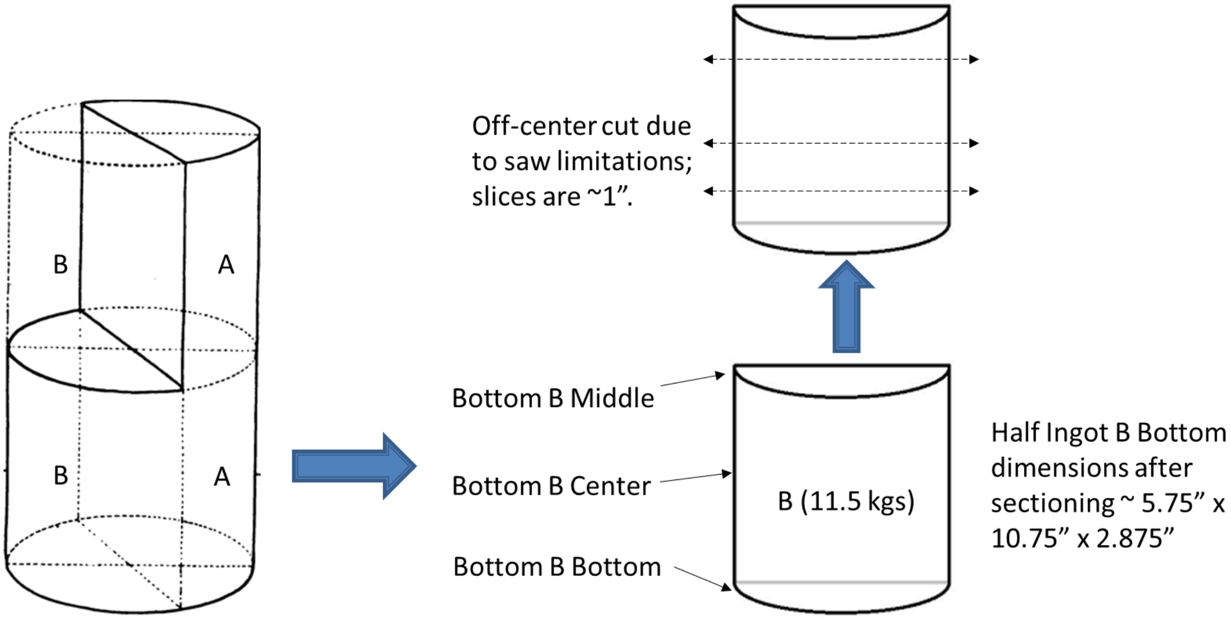

Fig. 3.7. Schematic of Ingot 1 cross-sectioning and sampling locations

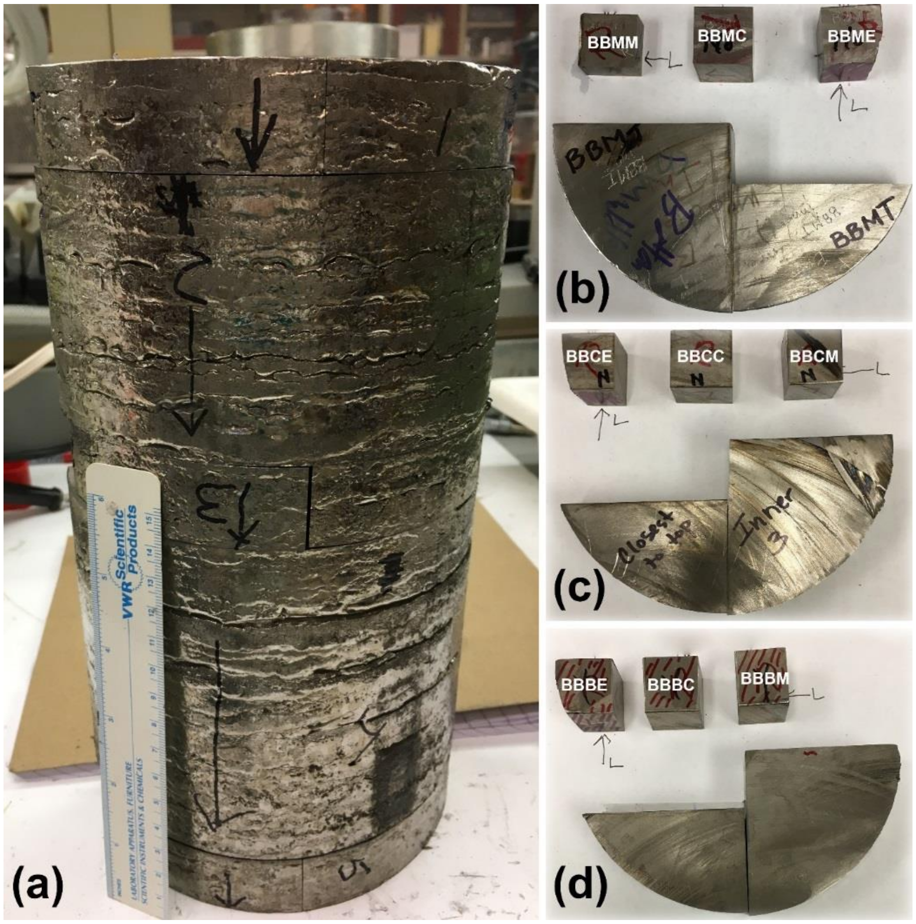

Fig. 3.8. Photograph of Ingot 1 (a) after sectioning, re-assembly and cross-sectioned (b) top, (c) middle and (b) bottom

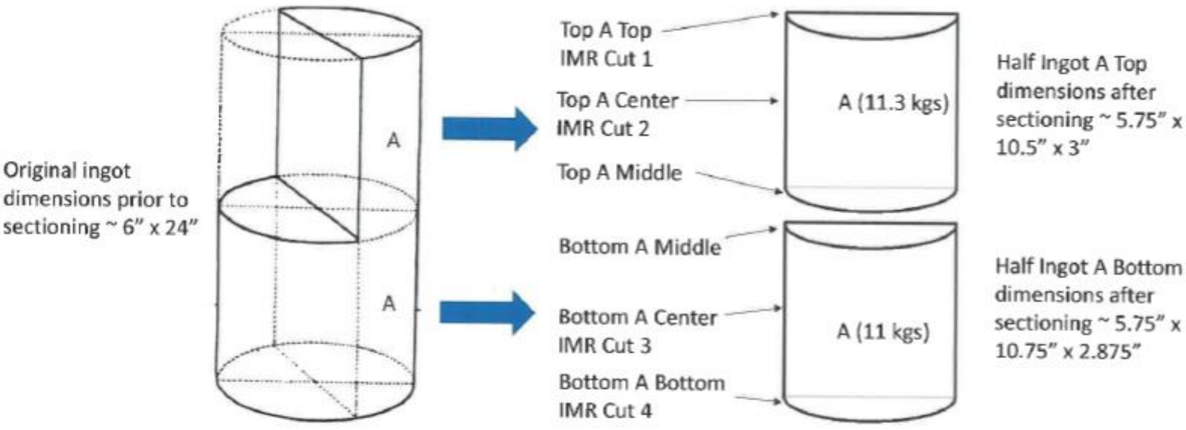

Fig. 3.9. Schematic of Ingot 1, Side "A" cross-sectioning and sampling locations

3.2.3 Macroscale Composition

3.2.3.1 Chemical Methods

The top and bottom "A" halves of Ingot 1 (Fig. 3.9) were sent to IMR Test Labs, Lansing, NY for sectioning and chemical analysis by ICP/MS, C, N, O, H and S analysis. Three samples each were taken from each slice near the center, mid-radius and edge for ICP-AES (Fig. 3.10), ICP-MS and IGF. The results are summarized in Table 3.4-6. IGF (LECO Corp.) results obtained at IMR Test Labs and LLNL (Table 3.6) are consistent for carbon, nitrogen, and oxygen and are inconsistent for hydrogen and sulfur. Note that no effort was made to remove carbon and oxygen from the alloyed ingots during CHM processing.

Table 3.4. Sample ID and locations

Sample Cut	Cut 1 Top A Top	Cut 2 Top A Center	Cut 3 Bottom A Center	Cut 4 Bottom A Bottom
Sample ID	• 1 Edge • 1 Mid-Radius • 1 Core	• 2 Edge • 2 Mid-Radius • 2 Core	• 3 Edge • 3 Mid-Radius • 3 Core	• 4 Edge • 4 Mid-Radius • 4 Core

Table 3.5. Elemental analysis of half of Ingot 1; locations indicated in Fig. 3.8 [18]

Element	**1 Edge**	**1 Mid-Radius**	**1 Core**	**2 Edge**	**2 Mid-Radius**	**2 Core**
Al	0.004	0.005	0.004	0.006	0.005	0.004
C[1]	0.02	0.02	0.02			
Cr	0.001	0.001	0.001	0.001	0.001	0.001
Fe	0.014	0.013	0.014	0.012	0.013	0.012
H[2]	0.001	0.001	0.001			
Mg	0.002	0.001	0.001	0.001	<0.001	0.001
Mo	0.001	0.001	0.002	<0.001	<0.001	0.001
N[2]	0.01	0.01	0.01			
Nb[3]	19.82	20.65	21.18	22.04	21.66	21.37
Ni	0.003	0.003	0.003	0.003	0.003	0.003
O[2]	0.08	0.08	0.08			
S[1]	0.002	0.001	0.002			
Sn	0.002	0.002	0.002	0.002	0.002	0.002

Ta	0.001	0.001	0.001	0.002	0.001	0.001
Ti[4]	80.03	79.21	78.67	77.93	78.31	78.60
Zr	0.005	0.005	0.005	0.005	0.005	0.005
Element	**3 Edge**	**3 Mid-Radius**	**3 Core**	**4 Edge**	**4 Mid-Radius**	**4 Core**
Al	0.004	0.004	0.022	0.005	0.004	0.004
C[1]						
Cr	0.001	0.001	0.001	0.001	0.001	0.002
Fe	0.013	0.014	0.018	0.014	0.017	0.018
H[2]						
Mg	<0.001	0.001	0.002	0.001	0.001	<0.001
Mo	<0.001	<0.001	0.001	<0.001	<0.001	<0.001
N[2]						
Nb[3]	22.95	22.66	22.73	18.09	18.22	18.31
Ni	0.003	0.002	0.003	0.003	0.004	0.004
O[2]						
S[1]						
Sn	0.002	0.002	0.002	0.002	0.002	0.002
Ta	0.002	0.001	0.002	0.001	0.001	0.001
Ti[4]	77.02	77.31	77.21	81.88	81.74	81.65
Zr	0.005	0.005	0.005	0.005	0.005	0.005

[1] **Determined by combustion-infrared absorbance**
[2] **Determined by IGF**
[3] **Determined by ICP-AES**
[4] **Determined by difference, excluding any gases that may be present**
Other elements tested (<0.01%): K, P, Pd & Si
Other elements tested (<0.001%): Ag, As, B, Ba, Be, Bi, Cd, Co, Cs, Cu, Ga, Ge, Hf, In, La, Li, Mn, Na, Pb, Rb, Re, Sb, Se, Sr, Te, Th, Tl, U, V, W & Zn
Results in weight percent unless otherwise indicated
Method(s): CAP-079B (ICP-MS), CAP-017Q (ICP-AES), ASTM E 1941-10 (2016) (Comb.), ASTM E 1447-09 (2016) (IGF), and ASTM E 1409-13 (IGF)

Table 3.6. Impurities measured at LLNL via IGF; results in μg/g

	C	H	N	O	S
BBMM	190.97	30.7	80.6	945	878
BBMC	182.67	42.7	78.3	928	812
BBME	190.97	32.5	85.3	1000	878
BBCM	198.64	58.8	88.6	919	821
BBCC	207.23	66.2	90.3	912	957
BBCE	201.6	57.2	85.7	919	733
BBBM	226.73	25.7	88.5	907	893
BBBC	212.03	24.4	86.3	867	850
BBBE	207	47.9	88.4	954	944

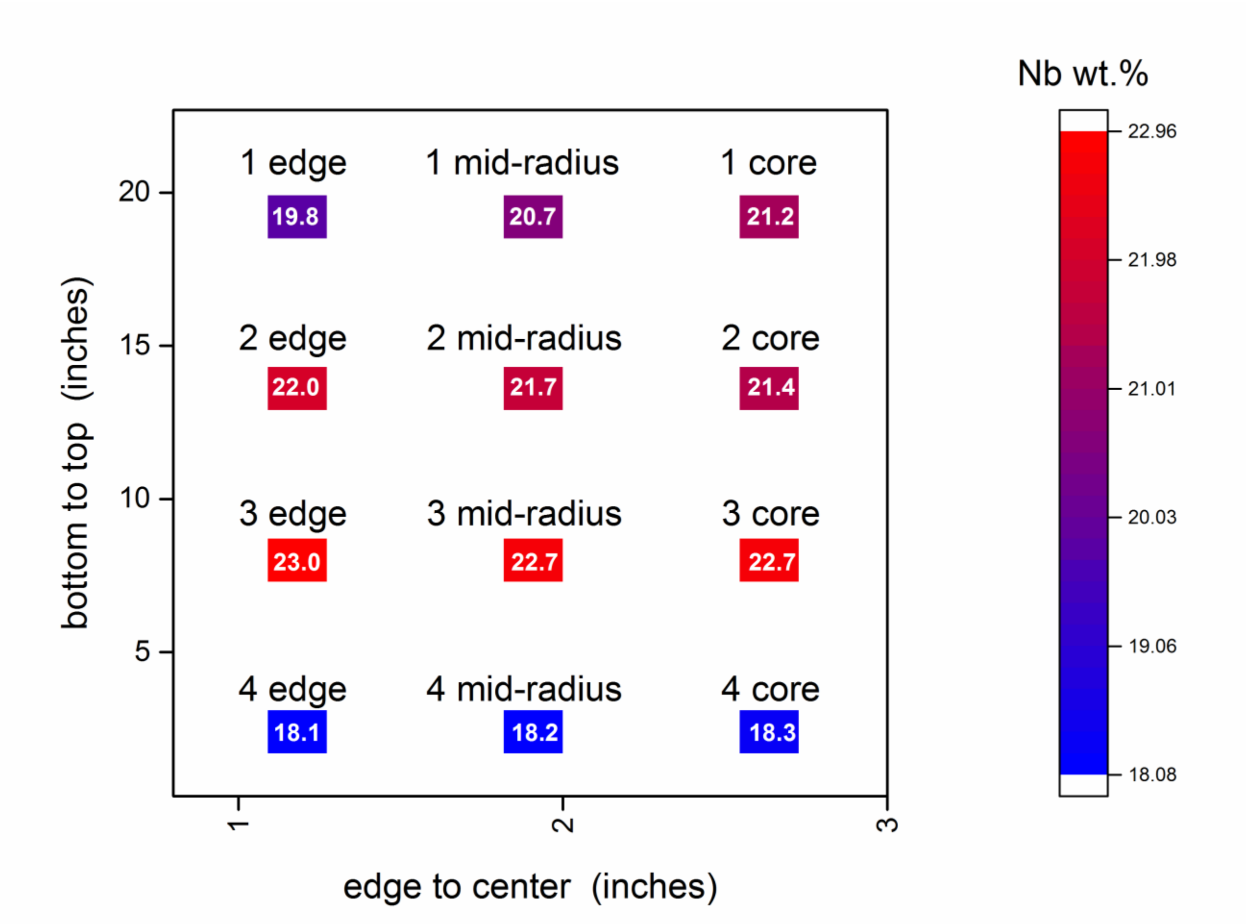

Fig. 3.10. Graph depicting ICP-AES measurements of Nb content from center to edge and bottom to top of Ingot 1, where red represents regions of high Nb and blue represents regions of low Nb content.

3.2.3.2 X-ray Fluorescence

A brief survey of Ingot 1 top surface, cut bottom surface and three wall locations via handheld XRF (Bruker S1 TITAN) resulted in measurements ranging from 25 to 32 wt.% (14.7-19.5 at.%) Nb. Note that this handheld XRF has a spot size of 5 mm and is routinely checked using reference standards and is operating within an acceptable regime for both Nb and Ti.

The ingot feedstock was analyzed at LLNL using a handheld XRF (Olympus Delta Professional Model DPO-2000-CC) calibrated using a 316L stainless steel reference standard. The outer surface composition of the filled Nb tube (Fig. 2.6) measured 100±0.25% Nb and the filled inner region measured 100±1.04% Ti at one end and 99.91% Ti at the other end. Both fill measurements were acquired 1” from the tube edge. The center of the tube composition was measured at 99.97% Ti and 0.03% Nb.

At LLNL, Ingot 1 cross-sectioned top surface “B” (shown in Fig. 3.7) was analyzed using. Results from this analysis are shown in the table in Fig. 3.11. While the range of Nb wt.% values corresponds to those measured via ICP-AES (Table 3.5, Fig. 3.11), the middle and top ingot radial measurements do not agree. The centerline ingot measurements do agree. This evidence points to banding, which will be discussed more in the next section.

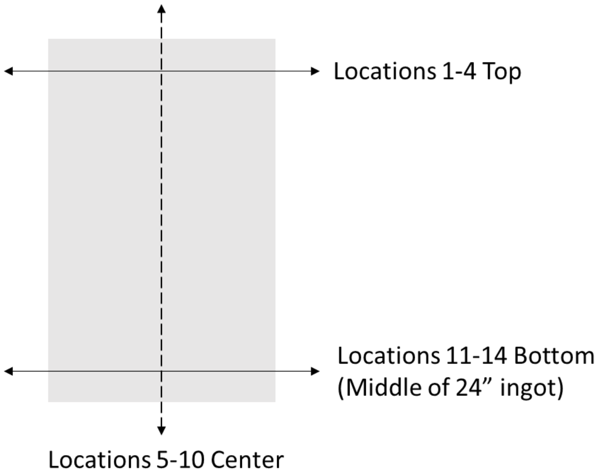

Measurements were taken ~ 1” from the top and bottom and down the center of the ingot at 1.25” intervals. Note ~2-3 wt.% decrease in Ti in the center of the ingot.

Location	Ti (wt. %)	Nb (wt. %)
1	81.7	18.3
2	81.5	18.5
3	81.1	18.9
4	81.5	18.5
5	79.3	20.7
6	76.3	23.7
7	76.4	23.6
8	78.9	21.1
9	77.7	22.3
10	80.3	19.7
11	80.9	19.1
12	81.9	18.1
13	81.3	18.6
14	81.5	18.5

Additional handheld XRF measurements were acquired at LLNL on various Ti-Nb samples. These are listed in Table 3.7.

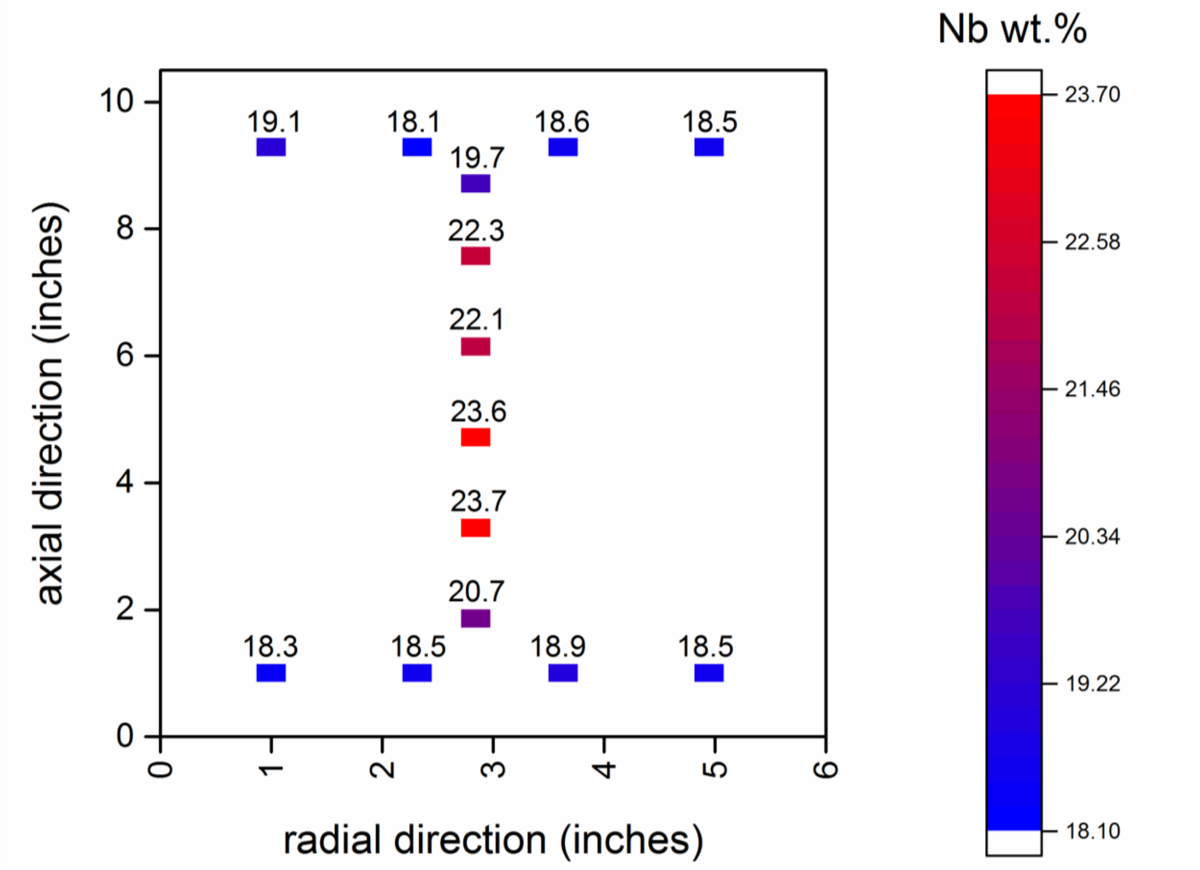

Fig. 3.11. Schematic depicting measurement locations across the top cross-sectional surface of Ingot 1 (upper left) and corresponding table of handheld XRF results (upper right). Results are plotted in a heat map (lower image), where red represents regions of high Nb and blue represents regions of low Nb and the axis is oriented along ingot edges.

Table 3.7. Handheld XRF measurements of Ti, Nb and impurities in the collected condensate and across Ingot 2

Sample	Ti	Cr	Fe	Mn	Ni	Cu	Nb
Condensate Area 1	96.86	0.58	1.42	0.37	.076	0.84	0.61
Condensate Area 2	91.32	1.62	4.56	0.53	0.025	0.091	1.63
Condensate Area 3	91.44	1.33	3.62	0.43	0.20	0.062	2.91
Large Condensate	93.03	0.88	4.96	0.35	0.72	0.050	
Ingot 2 Top	75.80						24.20
Ingot 2 Center	76.46						23.54
Ingot 2 Bottom	77.58						22.42

A Bruker M4 Tornado micro-XRF (spot size of 25µm, 50kV, 200µA Rh source) was also used to measure wt.% Nb. Note that, while these results have not been calibrated against a standard, they may serve as a means of describing the regional variation in Nb concentration. The results range from 20.4 to 25.7 wt.% Nb, corresponding to a range of 11.7 to 15.1 at.% Nb. An image of relative Nb banding (darkest region is 24 wt.% lightest is 13 wt.%) at the macroscale is shown in Fig. 3.12. Note the magnitude and length scale of the banding. This can potentially account for the difference in Nb concentration trends observed at different locations within Ingot 1 in the previous section.

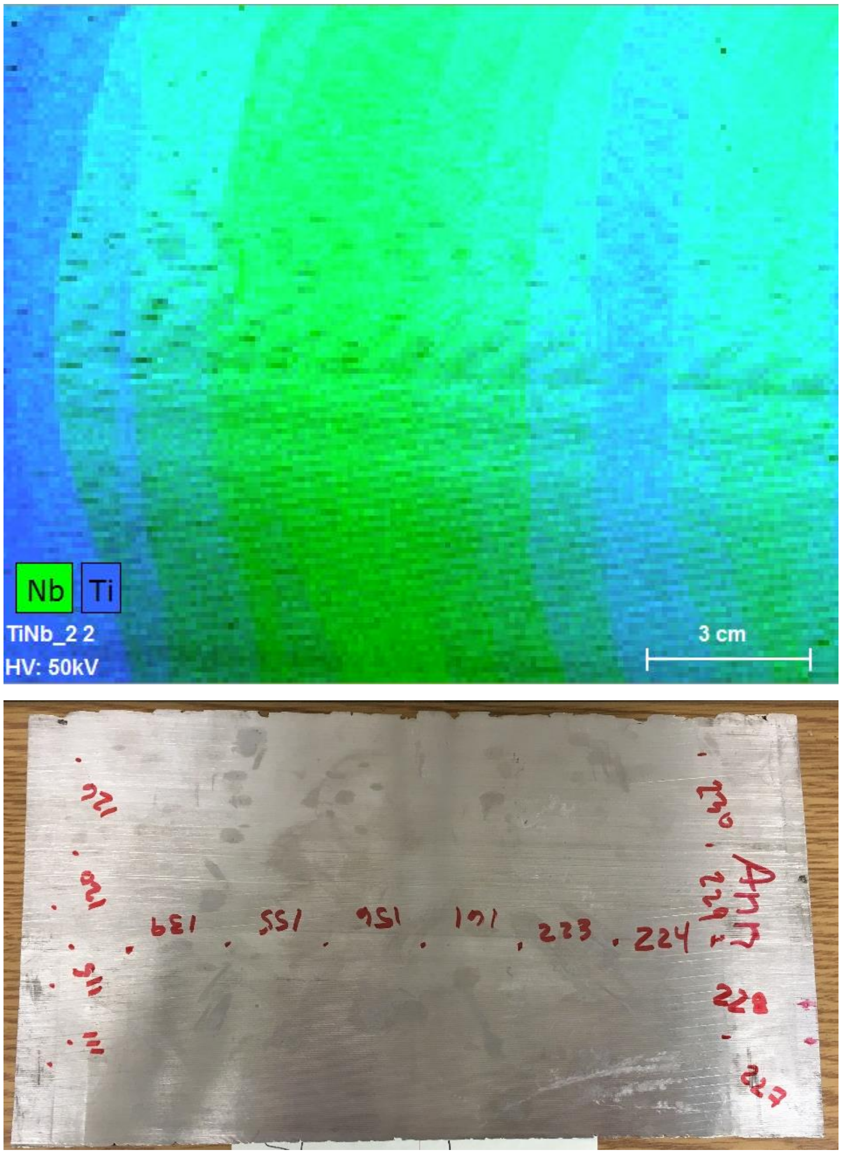

Fig. 3.12. XRF sampling across a 6” x 5” surface area of the axial cross-sectional surface of Ingot 1 (shown below in the same orientation at different scale) depicting high Ti (blue) and high Nb (green) regions.

3.2.4 Microscale Composition

Microscale variations in composition were measured using energy dispersive X-ray spectroscopy (EDS) and wavelength dispersive X-ray spectroscopy (WDS). EDS measurements were collected using a Philips XL30 SEM with electron beam parameters of 20 kV accelerating voltage, spot size 2 at 4000x magnification (Fig. 3.13). While macroscale differences in Nb concentration are observed (Fig. 3.12), no significant microscale variations in Nb distribution were observed across a 20 x 26 µm region (Fig. 3.14).

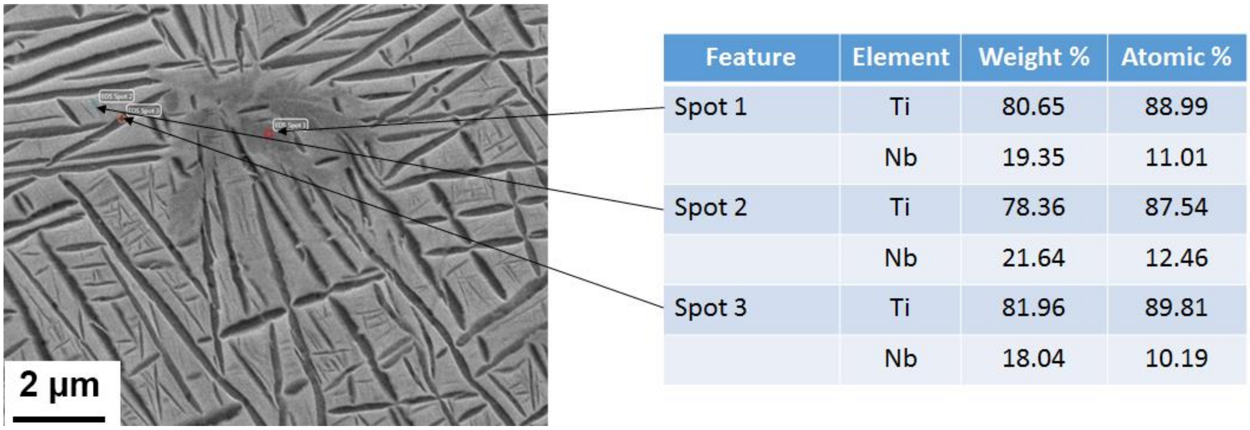

Feature	Element	Weight %	Atomic %
Spot 1	Ti	80.65	88.99
	Nb	19.35	11.01
Spot 2	Ti	78.36	87.54
	Nb	21.64	12.46
Spot 3	Ti	81.96	89.81
	Nb	18.04	10.19

Fig. 3.13. EDS measurements of Nb and Ti content obtained at three locations on the surface of a specimen machined from Ingot 1

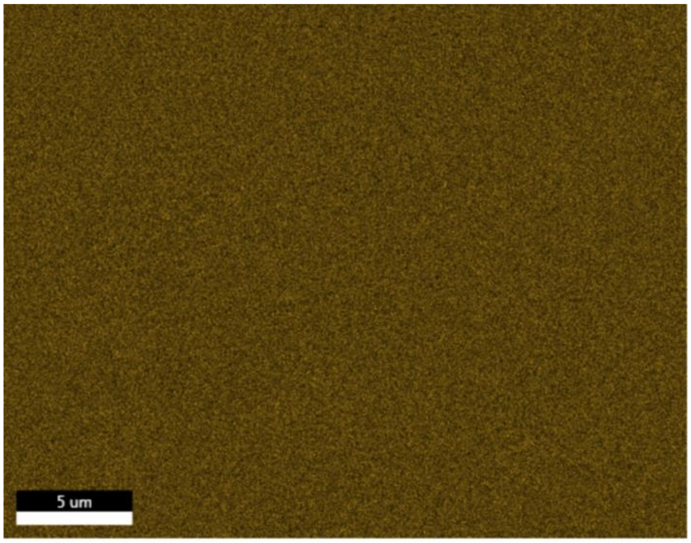

Fig. 3.14. EDS map of Nb content in a sample machined from Ingot 1; brown color representative of high Nb regions

Although these EDS results suggest compositional homogeneity at the microscale, solute segregation was observed with WDS. WDS measurements were conducted using a Jeol 8530F electron microprobe analyzer with electron beam parameters of 15 kV accelerating voltage and 50 nA beam current. Microscale composition variation appeared to correspond to the two-phase microstructure; low-contrast alpha lath-shaped precipitates, observed with BSE imaging, are lower in Nb concentration than the surrounding matrix

(Fig. 3.15). The difference between EDS and WDS results highlights the superior capability of WDS for quantitative spatial analysis of composition.

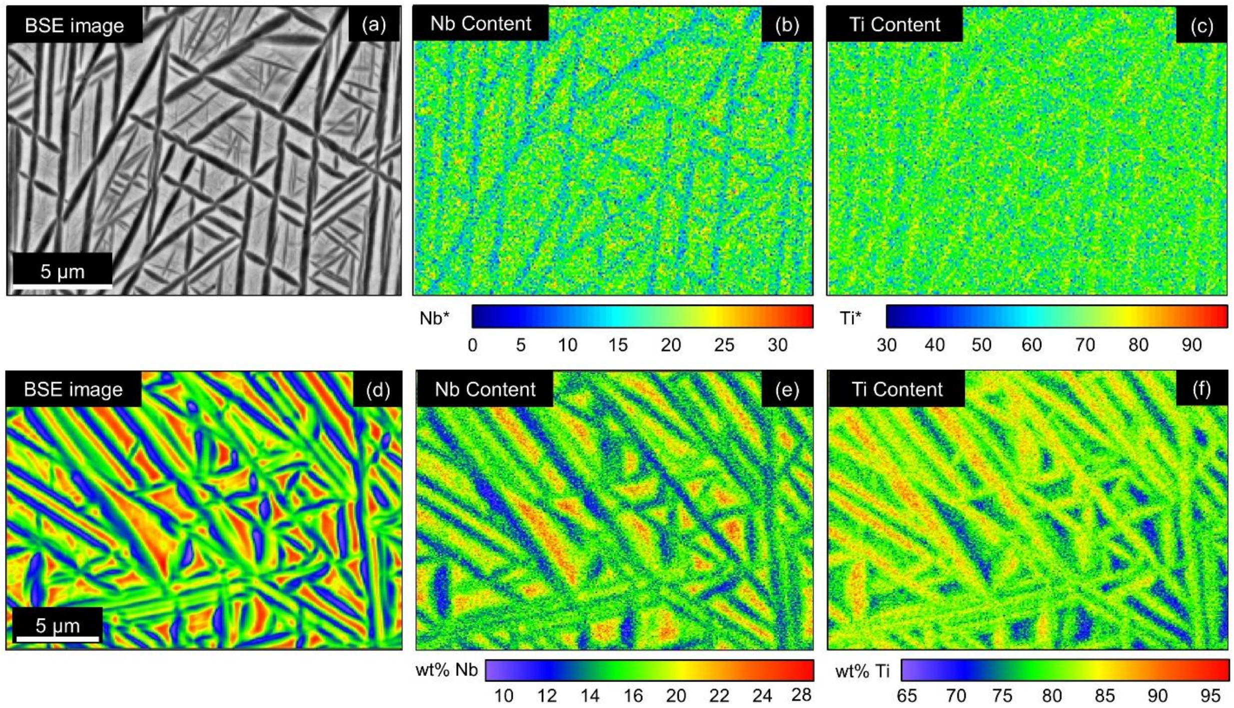

Fig. 3.15. WDS composition maps of Nb and Ti content of samples machined from Ingot I. (a-c) and (d-f) show two areas from specimen BBBC and BBMC, respectively, which were both machined from Ingot 1. (a) and (d) are backscattered electron images, (c) and (e) are maps of Nb content and (c) and (f) are maps of Ti content. In both regions, compositional segregation corresponds with the two-phase microstructure.
***The color bar scale in (b) and (c) is represented in arbitrary units of X-ray intensity, rather than weight percent. Despite this, (b) and (c) still give a qualitative view of spatial variation in Nb content.**

Line profiles of Nb composition were measured using WDS for four Ingot 1 specimen (BBBC, BBBE, BBMC and BBME) and are shown in Fig. 3.16. Each profile was measured over a length of 1 mm using a step size of 5 µm. The standard deviation of each profile is shown in Fig. 3.17. Greater microscale compositional variation was observed in center of the ingot compared to the bottom (refer to Figs. 3.7 and 3.8 for general specimen location within Ingot 1). Average standard deviation in Nb content was 1.17 wt % Nb greater at the center of the ingot (BBMX) compared to ingot bottom (BBBX), indicating that microscale solute segregation, in addition to macroscale composition (Fig. 3.12), varies spatially within Ingot 1. Profile averages from the ingot center specimen are ***less*** than those of the ingot bottom specimen (18.0 wt % Nb for both BBMC and BBME compared to 19.2 and 20.7 wt % Nb for BBBC and BBBE), which does not agree with XRF results (Fig. 3.11). This discrepancy could possibly be due to the difference in analysis length scale. Segregation yet may be observed at smaller length scales. Future efforts to characterize this alloy will involve nanoscale characterization via transmission electron microscopy.

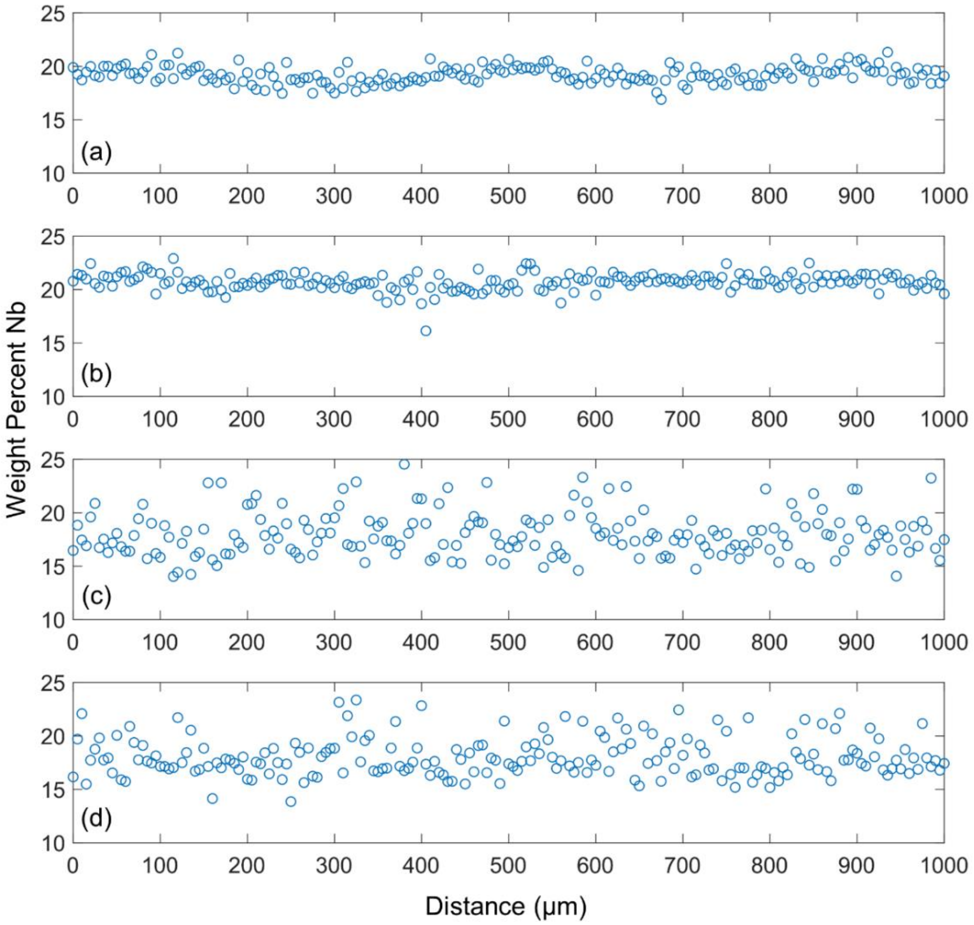

Fig. 3.16. Line profiles of Nb composition from (a) BBBC, (b) BBBE, (c) BBMC and (d) BBME specimen machined from Ingot 1. Each line profile measures a 1 mm distance with step size of 5 µm. Measurement error is +/- 0.05 wt % Nb.

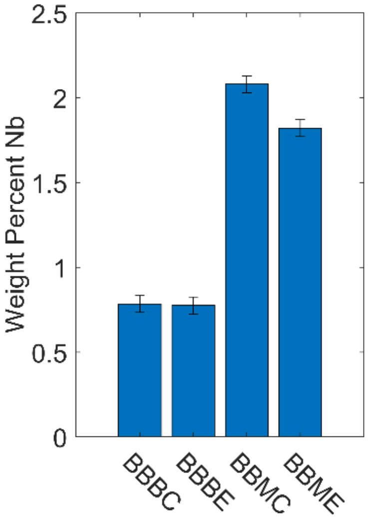

Fig. 3.17. Standard deviation of the Nb composition line profiles in Fig. 3.16.

3.2.5 Microstructure

Nine specimens were machined from Ingot 1, forming a matrix from axial center to edge and top to bottom (Fig. 3.8). These specimens were potted in epoxy resin then polished according to standard metallographic practices and etched by swabbing for 10 seconds with hydrofluoric and nitric acid (Kroll's etchant) to reveal grain boundaries and alpha and beta structures. During casting, the top surface of the ingot is continuously heated via EB, which specifically rasters around the circumference of the ingot, preventing solidification at the water-cooled crucible wall. This action prevents radial solidification shrinkage which can entrain voids during crucible filling and enforces axial/longitudinal heat flow. Grain growth occurs parallel to the direction of heat flow, as evidenced by the elongated grain structure observed in the radial direction (Fig. 3.18a) and equiaxed grain structure in the ingot draw direction (Fig. 3.18b). More on phases and microstructural features will be presented in a subsequent report.

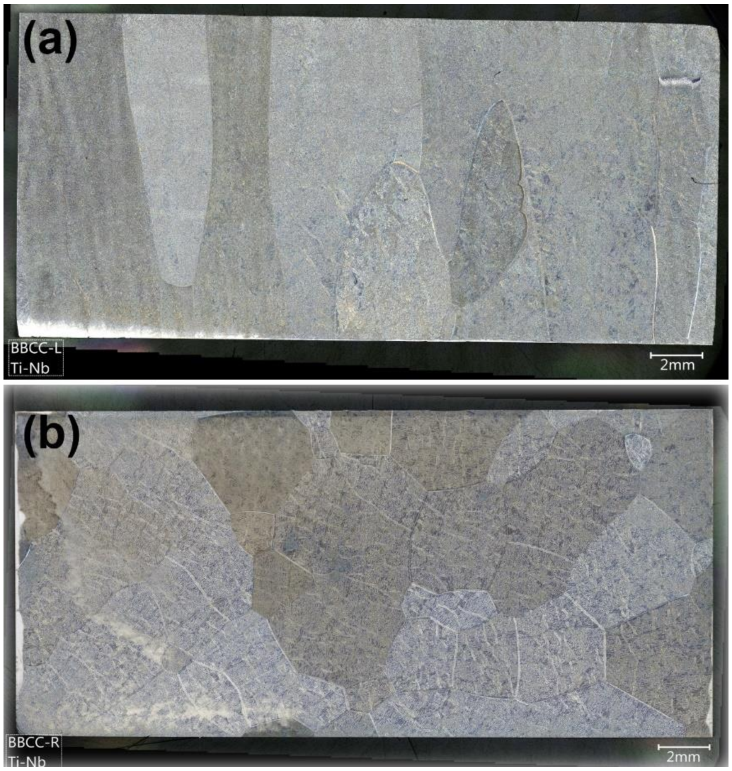

Fig. 3.18. Optical micrographs depicting microstructure in the (a) radial direction and (b) ingot draw direction in specimens machined from the center of the lower half of Ingot 1

3.3 Comments on Alloying via CHM

Trends in compositional gradients indicate that Nb concentration is greatest at the center of the ingot and lowest near the ingot walls. This may indicate that solidification progressed from the center to the edge of the ingot. At first, the solidified material will be Nb rich; see phase diagram (Fig.1.1). This progression is consistent with the heating strategy employed. The EB was rastered around the edge of the ingot, preventing edge-to-center solidification to prevent solidification shrinkage. The Nb distribution has been measured using different methods, including chemical (ICP-AES) and spectroscopic (EDS, XRF) techniques. The results indicate that the Nb composition varies globally with location across the alloyed ingot and that this variation is reasonably low, ranging from 2 to 5 at.%. This indicates that, at a first pass, EB CHM is a viable method to alloy Ti and Nb without requiring additional melting steps to improve alloy homogeneity. If this technology is used to provide refined feed for a vacuum arc remelt (VAR) furnace, then greater compositional gradients may be acceptable. If the EB is used to provide refined feed for shape casting, then large compositional gradients may be acceptable as long as the overall niobium content is at the target amount and there are no pockets of free niobium.

Based on this effort, modifications to the LLNL CHM system and operation to improve alloying include:

- Improved melting of Nb tube or consideration of alternative feedstock geometries to melt and deliver a uniform stoichiometric ratio of Ti and Nb to the hearth for alloying,
- Better control of feedstock delivery rate, which varies when the unattached ends of a mostly consumed feedstock rod/tube are dropped into the hearth, and
- Modified EB rastering pattern size and dwell time to improve melting of the Nb-rich hearth sidewall [15].

Section 4

Scrap Processing

Recycling of titanium scrap is a common practice in the EB CHM industry [9, 19, 20]. This demonstration is aimed at (1) evaluating melt losses using specific scrap geometry and (2) demonstrating scrap feed using a bar feeder. The latter evaluation could eliminate the need for a scrap feeder, which would save cost, maintenance time and facility space.

4.1 Scrap Preparation

A contoured part, similar to a hollow hemisphere, was fabricated from titanium and size-reduced using a Piranha (Megafab Ironworkers P-150) into the following forms:

- Scrap: 3/16-inch thick Ti sheet sheared to a <2.75” equivalent diameter and
- Coins: 3/16-inch thick Ti sheet punched to 2.5” and 2.75” D)

The remaining perforated metal (“porous scrap”) was further sheared into pieces roughly 3” or smaller.

4.2 Scrap Processing via CHM

4.2.1 Bar Feeder “Cold” Testing

4.2.1.1 Uncontrolled Scrap Loading

During cold trials (in which no melting occurred), 9846 kg of irregular Ti sheet material was loaded into the bar feeder. Filling the bar feeder in an uncontrolled manner (Fig. 4.1) resulted in jamming during the scrap delivery process. Aside from jamming, material delivery was inconsistent, varying from periods of no scrap feed and periods of bulk scrap release.

4.2.1.2 Stacked Scrap Loading

Stacking the scrap and coins on edge, as shown in Fig. 4.2, resulted in nearly complete scrap delivery without excessive jamming. The coins nested together; the porous scrap did not. For both scrap types, the titanium melted at the top, causing the scrap to adhere together. This prevented the scrap pieces from individually dropping into the melt pool, which is desirable for uniform melting. On occasion, large agglomerates formed which stuck to the side of the hearth or dropped to the bottom of the furnace chamber.

Fig. 4.1. Photographs of titanium scrap loaded into the bar feeder chamber (left) and delivery into a box (right)

Fig. 4.2. Bar feeder loaded with coin material

4.2.2 Bar Feeder "Hot" Testing

Scrap rotated during feeding, resulting in minor jamming at the bar feeder chute [15]. Nevertheless, scrap was melted with melt losses of <4% (Table 4.1). During melting, the material clumped up within the feed tube (Fig. 4.3); however, the drive never stalled out. This binding caused some scrap to overflow outside the edges of the hearth (Fig. 4.4). An ingot processed from scrap fed in this manner is shown in Fig. 4.4 and 4.5.

Fig. 4.3. Photographs of scrap melting in the ALD CHM furnace

Fig. 4.4. Photographs of the CHM chamber after scrap melting depicting the ingot withdrawal mechanism in the ingot removal position (left) and un-melted scrap and coins built up before the hearth and lying on the chamber floor after falling off the edge (right)

Fig. 4.5. Photograph of ingot produced from recycled scrap

Table 4.1. Scrap melting mass balance [15]

Item	Input mass (g)	Output mass (g)
Ti scrap feedstock, irregular	9846	782
Ti scrap feedstock, 2.5" D	6981	1559
Ti scrap feedstock, 2.75" D	1179	0
Ti ingot starter	5600	6881
Hearth skull + splash		13471
Total	23606	22693
% Loss	3.9	

4.3 Comments on Scrap Processing

The scrap feeding test demonstrated a potential ability to feed in scrap and coins via a bar-feeder. Several opportunities to improve scrap and coin feeding were identified during this test. First, the feed conveyor area delivering material to the hearth can be modified to better direct material. Second, the single bar feed mechanism used on ALD’s in-house system does not directly represent LLNL’s proposed multi-bar feed system; there are several complexities involved with the indexing aspect of LLNL’s feeder. Collaborations between the LLNL and ALD teams resulted in design concepts which should promote successful scrap feeding via an indexing bar-feeder. ALD took the action to finalize these designs for LLNL review and approval.

In conclusion, two key elements must be considered on LLNL’s bar feeder to ensure successful scrap and coin feeding. First, using a guide to direct the material into the hearth is advantageous; this can be retrofitted as needed by LLNL. Second, minimizing the gaps within the bar feed delivery system is necessary to prevent material hang-ups and binding.

Appendix A

Powder Consolidation

A feasibility assessment to recycle waste material in the form of powder was performed using EB CHM. Laser powder bed fusion additive manufacturing (AM) generates small amounts of waste in the form of oversized powder and build scrap (e.g. lattice support structure) and CHM may be able to recycle this waste material. Spherical, 50-75 µm diameter 316L stainless steel powder and AM support structures were provided for this three-part demonstration [21].

Powder Trial 1: Direct Feed

Stainless steel powder was delivered into the CHM chamber using an overhead vibratory feed attachment equipped with a guide tube. EB melting of powder using this delivery method was attempted multiple times, with the undesirable result of powder dispersal across the CHM chamber. The electrostatic loading of the powder, even after reducing the emission current caused the powder to disperse. The observed spreading of the powder lead to tremendous material losses. After these unsuccessful melt attempts, the powder was found at the bottom of the melt chamber even in the furnace pre pump line [15].

Powder Trial 2: Melting using Consolidation Hearth

Stainless steel powder was melted within a consolidation hearth to create a slab casting. After EB melting, 10% of the starting powder was found in a melted form in the crucible the remaining 90% was finely distributed along the melt chamber [15].

Powder Trial 3: Scrap and Powder Melting using Consolidation Hearth

A mixture of powder and solid AM support structure was packed into a consolidation hearth, with the powder sandwiched between solid AM support structure. Melting proceed in a reasonable and uniform manner, but partway through the melt some powder was ejected through the molten layer on top of the hearth. Upon removal of the melted and uncast metal from the hearth, loose powder was observed at the edges and bottom of the plate. A material loss of 11 g or 0.12% was realized (Table A.1).

Powder Melting Mass Balances

Some powder was recovered from the chamber and could potentially be reprocessed. This is indicated in Table A.1. Powder lost includes vaporized material and powder lost to the chamber.

Table A.1. Powder recycling feasibility assessment mass balances, all measurements in g unless otherwise noted [21]

	Powder Trials		
	Trial 1	Trial 2	Trial 3
Input powder	7466	9312	8820
Ingot	2000	420	8001
Recovered	4572	4624	808
Cast %	26.7	4.5	90.7
Lost %	12.0	45.8	0.12

Comments on Powder Processing

EB CHM may provide a viable method for consolidating and recycling scrap produced by AM. However, the high vacuum and LLNL machine configuration preclude U-6Nb processing. U-6Nb powder presents additional hazards in the form of powder reactivity and radioactivity, which make any powder distribution in the chamber (or unmelted powder clinging to the solidified hearth metal) highly undesirable [22].

Appendix B

References

1. McKoon, R.H. *Scrap Uranium Recycling via Electron Beam Melting*. in *Electron Beam Melting and Refining Conference*. 1993. Reno NV.
2. McKoon, R.H., *Progress Toward Uranium Scrap Recycling via Electron Beam Cold Hearth Refining*, in *Proceedings of the Conference on Electron Beam Melting and Refining - State of the Art 1994*, R. Bakish, Editor. 1994, Bakish Materials Corp: Englewood. p. 130-140.
3. McKoon, R.H. *Characterization of U-6Nb Ingots Produced via the Electron Beam Cold Hearth Refining Process*. in *Electron Beam Melting and Refining State of the Art 1997 Conference*. 1997. Reno NV.
4. Wu, A.S., T.P. Pluschkell, R.H. McKoon, T. Boutaleb, M.W. Wraith, S.C. Burke, S.K. Allen, and W. Mclean, *Electron beam cold hearth melt system statement of work and specification document (LLNL-PROP-751197)*. 2018, Lawrence Livermore National Laboratory.
5. Bönisch, M., *Structural Properties, Deformation Behavior and Thermal Stability of Martensitic Ti-Nb Alloys*, in *Fakultat Mathematik und Naturwissenschaften*. 2016, Technischen Universit• at Dresden.
6. Jackson, R.J., *Rocky Flats Technical Datasheet (RFP-1613), Uranium-6 wt. pct. Niobium Material Properties*. The Dow Chemical Company. 1971.
7. Roehling, J.D., A. Perron, J.-L. Fattebert, T. Haxhimali, G. Guss, T.T. Li, D. Bober, A.W. Stokes, A.J. Clarke, P.E.A. Turchi, M.J. Matthews, and J.T. McKeown, *Rapid Solidification in Bulk Ti-Nb Alloys by Single-Track Laser Melting.* Journal of Materials, 2018. **70**(8): p. 1589-1597.
8. Li, Y., J. Li, and B. Liu, *The Atomistic Mechanism of HCP-to-BCC Martensitic Transformation in the Ti-Nb System Revealed by Molecular Dynamics Simulations.* Physical Chemistry Chemical Physics, 2015. **17**(6): p. 4184-4192.
9. Dietrich, W. and H. Stephan, *Electron Beam Melting and Casting*, in *ASM Handbook*, D.M. Stefanescu and J.R. Davis, Editors. 1988. p. 410-419.
10. Hackenberg, R.E., D.W. Brown, A.J. Clarke, L.B. Dauelsberg, R.D. Field, W.L. Hults, A.M. Kelly, M.F. Lopez, D.F. Teter, D.J. Thoma, T.J. Tucker, C.J. Vigil, and H.M. Volz, *U-Nb Aging Final Report (LA-14327)*. 2007, Los Alamos National Laboratory: Los Alamos NM.
11. McKoon, R.H. *Decarburization of Uranium Via Electron Beam Processing*. in *Electron Beam Melting and Refining State of the Art 1998*. 1998. Reno NV.
12. Smith Jr., H.R., *Purification of Metals*. 1963, United Metallurgical Corp.: United States.
13. Honig, R.E., *Vapor Pressure Data for the More Common Elements.* RCA Review, 1957. **18**: p. 195-204.
14. Harker, H.R. and C.H. Entrekin, *Electron Beam Cold Hearth Refining*. 1989, Titanium Health Technologies, Inc.: United States.
15. Flinspach, J., *Preliminary Functionality Trials Report for EB 1-50-600 Project*. 2019, ALD Vacuum Technologies GmbH.
16. Wu, A.S., *Notes from Preliminary Functionality Trials at ALD*. 2019: Hanau, Germany.
17. McMenomey, J., *Electron Beam and Plasma Arc Melting and Refining*, A. Wu and K. Blobaum, Editors. 2017: Ukiah, CA.
18. *IMR Report Number 201913540*. 2019, IMR Test Labs.
19. Powell, A., J. Van den Avyle, B. Damkroger, J. Szekely, and U. Pal, *Analysis of Multicomponent Evaporation in Electron Beam Melting and Refining of Titanium Alloys.* Metallurgical and Materials Transactions B-Process Metallurgy and Materials Processing Science, 1997. **28**(6): p. 1227-1239.

20. Choudhury, A. and E. Hengsberger, *Electron-Beam Melting and Refining of Metals and Alloys*. ISIJ International, 1992. **32**(5): p. 673-681.
21. Pluschkell, T.P., *LLNL Preliminary Functionality Trials (PFT) 316L Oversized Powder At ALD*. 2019: Lawrence Livermore National Laboratory. p. 1-6.
22. DeMint, A., *Visit to ALD Vacuum Technologies, Hanau, Germany, June 17-27, 2019*. 2019, Y-12 National Security Complex.